Journal of Computational Physics 229 (2010) 7609–7624

Contents lists available at ScienceDirect

Journal of Computational Physics

journal homepage: www.elsevier.com/locate/jcp

Computation of three-dimensional Brinkman flows using regularized methods

Ricardo Cortez [a,*], Bree Cummins [a], Karin Leiderman [b], Douglas Varela [c]

[a] Mathematics Department, Tulane University, New Orleans, LA 70118, USA
[b] Mathematics Department, University of Utah, Salt Lake City, UT 84112, USA
[c] DVC Pasadena, CA, USA

ARTICLE INFO

Article history:
Received 8 January 2010
Received in revised form 27 May 2010
Accepted 8 June 2010
Available online 19 June 2010

Keywords:
Brinkman equations
Regularization
Fundamental solution

ABSTRACT

The Brinkman equations of fluid motion are a model of flows in a porous medium. We develop the exact solution of the Brinkman equations for three-dimensional incompressible flow driven by regularized forces. Two different approaches to the regularization are discussed and compared on test problems. The regularized Brinkman model is also applied to the unsteady Stokes equation for oscillatory flows since the latter leads to the Brinkman equations with complex permeability parameter. We provide validation studies of the method based on the flow and drag of a solid sphere translating in a Brinkman medium and the flow inside a cylindrical channel of circular cross-section. We present a numerical example of a swimming organism in a Brinkman flow which shows that the maximum swimming speed is obtained with a small but non-zero value of the porosity. We also demonstrate that unsteady Stokes flows with oscillatory forcing fall within the same framework and are computed with the same method by applying it to the motion of the oscillating feeding appendage of a copepod.

1. Introduction

A Brinkman medium is a homogeneous porous medium characterized by a permeability parameter, α^{-2}. The Brinkman equations represent a viscous fluid flow through a cloud of spherical particles whose size is smaller than the characteristic length scale of the flow, and therefore occupy a negligible volume [6]. Viscous flow in a porous medium is accurately described by the Brinkman equations for incompressible flow

$$\frac{\mu}{K}\mathbf{u}^* = -\nabla p^* + \mu\Delta\mathbf{u}^* + \mathbf{F}^*, \quad \nabla\cdot\mathbf{u}^* = 0,$$

where $\mathbf{u}^* = (u, v, w)$ is the average fluid velocity, p^* is the average fluid pressure, μ is the dynamic viscosity, K is the Darcy permeability of the medium and $\mathbf{F}^*$ is the body force density. The superscript indicates dimensional quantities. The averages are assumed to occur over many realizations of particle arrangements that satisfy the permeability, particle size, and volume fraction constraints of the porous medium [6,13]. The equation indicates that, in the absence of forces, the Darcy term $\mu/K\mathbf{u}^*$ and the diffusion balance the pressure gradient. We write the equations in dimensionless form by defining a particle length scale L, velocity scale U, pressure scale $\mu U/L$ and a force scale $\mu U/L^2$ to write

$$\alpha^2\mathbf{u} = -\nabla p + \Delta\mathbf{u} + \mathbf{F}, \quad \nabla\cdot\mathbf{u} = 0,$$

* Corresponding author. Tel.: +1 504 862 3436; fax: +1 504 865 5063.
E-mail address: cortez@math.tulane.edu (R. Cortez).

0021-9991/$ - see front matter © 2010 Elsevier Inc. All rights reserved.
doi:10.1016/j.jcp.2010.06.012

where the dimensionless parameter $\alpha = L/\sqrt{K}$ represents the ratio of the particle dimension to the permeability length scale of the medium.

The assumption is that α is small enough that the diffusion term is significant and Darcy's law alone does not apply. Notice that as $\alpha \to 0$, the Brinkman equations reduce to the Stokes equations. For bodies moving in a Brinkman medium, the permeability parameter provides a relative weight of the Darcy drag and Newtonian viscous drag. For instance, the drag force experienced by a stationary rigid sphere of radius a in a uniform Brinkman flow $\mathbf{U}$ was given by Brinkman [2] as

$$F_{drag}(\alpha) = 6\pi\mu a|\mathbf{U}|(1+\alpha+\alpha^2/3),$$

so that the terms containing α can be seen as corrections to the Stokes drag for small α. Although the drag on the sphere increases as α increases, this is not necessarily the case for oscillating filaments swimming in a Brinkman fluid, as is discussed in Section 3.4.

The Brinkman equations have been used to model the diffusion of small molecules through the loose fibrous glycocalyx that surrounds the endothelial cells lining capillary walls [7,21], as well as the flow through an array of fixed fibers [9] and Stokes flow over permeable aggregates [23]. An inflexible porous medium, such as one composed of rigid, fixed cylinders, is associated with values of $\alpha < O(1)$. More flexible media like the glycocalyx of cells may have $\alpha \approx O(10)$ or greater [7]. In [18], the authors consider resistivities R of biological materials in the range $2\times10^5 - 10^8$ dyn s/cm^4, with glycocalyx in the middle of the range. The resistivity is defined as $R = \mu/K$ which gives values of $K \in [10^{-12}, 5\times10^{-8}]$ cm^2 based on plasma viscosity of $\mu = 0.01$ dyn s/cm^2. For particle size of $L = 1$ μm, the corresponding range for α is $[0.4, 100]$. Here we consider $\alpha \in [0, 100]$ to include the Stokes limit.

We present a numerical method for calculating flows within a Brinkman medium subject to external forcing. The forces may be distributed throughout the fluid in any manner, but the motivation for the technique lies in its application to moving interfaces or slender bodies within a three-dimensional fluid domain. When the object of interest in the Brinkman medium is a curve or collection of points, then the integral expression based on Green's functions is singular. This scenario occurs when studying the motion of a slender body, such as bacterial flagella or helical swimmers [13]. Our method of regularized fundamental solutions is similar to that developed for the Stokes equations [4].

A numerical method for the solution of Brinkman equations based on the boundary integral formulation of the problem can be found in [7]. That work is restricted to axisymmetric problems where the boundaries are generated by rotating contours about a common axis. This symmetry allows part of the surface integrals to be done exactly and compute only one-dimensional weakly singular integrals. The latter are done via a change of variables that concentrates Gaussian quadrature points near the singularities. The result is a highly accurate method for that class of problems. Other approaches to the numerical solution of the Brinkman equations with acceleration terms (Navier–Stokes–Brinkman) use a finite-volume discretization of the differential equations [24,10].

1.1. Model equations

From now on, we set the viscosity to $\mu = 1$ since it can be scaled out of the equations. We consider first a force $\mathbf{F}$ given by a single regularized force centered at the origin:

$$\mathbf{F}(\mathbf{x}) = \mathbf{f}\phi_\delta(\mathbf{x}),$$

where $\mathbf{f}$ is a constant vector coefficient. Here we assume that the blob ϕ_δ is a radial function (i.e. $\phi_\delta = \phi_\delta(r)$) and that it satisfies $4\pi\int_0^\infty r^2\phi_\delta(r)dr = 1$. The blob (or cutoff function) can be thought of as a narrow Gaussian whose width is controlled by a small positive parameter δ such that $\phi_\delta(\mathbf{x})$ approaches a delta distribution as $\delta \to 0$. Assuming there are no boundaries, we take the divergence of the general equation to find

$$\Delta p = \mathbf{f}\cdot\nabla\phi_\delta \Rightarrow p = \mathbf{f}\cdot\nabla G_\delta \Rightarrow \nabla p = (\mathbf{f}\cdot\nabla)\nabla G_\delta,$$

where $\Delta G_\delta = \phi_\delta$ with $G_\delta \to 0$ as $r \to \infty$. This is exactly the same expression as for Stokes flow. Now the velocity satisfies

$$(\alpha^2 - \Delta)\mathbf{u} = [\mathbf{f}\phi_\delta - (\mathbf{f}\cdot\nabla)\nabla G_\delta].$$

We define B_δ implicitly as the solution of

$$(\Delta - \alpha^2)B_\delta = G_\delta, \tag{1}$$

also with a zero boundary condition at infinity, so that the fluid flow has the representation formula

$$\mathbf{u} = (\mathbf{f}\cdot\nabla)\nabla B_\delta - \mathbf{f}\Delta B_\delta. \tag{2}$$

If the blob $\phi_\delta(r)$ is a radial function, then both $G_\delta(r)$ and $B_\delta(r)$ are also radial. This allows us to write Eq. (1) as

$$[rB_\delta(r)]'' - \alpha^2[rB_\delta(r)] = rG_\delta(r), \tag{3}$$

which reduces Eq. (2) to

$$\mathbf{u}(\mathbf{x}) = \mathbf{f}H_1(r) + (\mathbf{f}\cdot\mathbf{x})\mathbf{x}H_2(r), \tag{4}$$

where the functions

$$H_1(r) = -\frac{rB_\delta'' + B_\delta'}{r}, \quad H_2(r) = \frac{rB_\delta'' - B_\delta'}{r^3},$$

contain the regularization.

1.2. The singular expressions ($\delta \to 0$)

The singular case is equivalent to the case when the blob is replaced by a delta function. In that case, the resulting expressions are

$$G(r) = \frac{1}{4\pi r}, \quad B(r) = \frac{1 - e^{-\alpha r}}{4\pi\alpha^2 r}.$$

These lead to the known expressions

$$H_1(r) = \frac{e^{-\alpha r}}{4\pi r}\left(\frac{1}{\alpha^2 r^2} + \frac{1}{\alpha r} + 1\right) - \frac{1}{4\pi\alpha^2 r^3},$$
$$H_2(r) = -\frac{e^{-\alpha r}}{4\pi r^3}\left(\frac{3}{\alpha^2 r^2} + \frac{3}{\alpha r} + 1\right) + \frac{3}{4\pi\alpha^2 r^5}.$$

Throughout this paper, we will refer to Eq. (4) as a *regularized Brinkmanlet* when $\delta > 0$ and as a *Brinkmanlet* in the singular case.

1.3. The fluid velocity

Eq. (4), which may be written succintly as $\mathbf{u}(\mathbf{x}) = K_B^\delta(\mathbf{x} - \mathbf{x}_0)\mathbf{f}$ gives the velocity field at a point $\mathbf{x}$ due to a force $\mathbf{f}$ located at $\mathbf{x}_0$. In the case of a flow generated by N forces at different locations, the linearity of the equations leads to the superposition

$$\mathbf{u}(\mathbf{x}) = \sum_{k=1}^{N} K_B^\delta(\mathbf{x} - \mathbf{x}_k)\mathbf{f}_k. \tag{5}$$

There are cases of interest where a body or a filament moves in a Brinkman fluid. In those cases, the forces are located either on the surface Σ of the body or along the filament Γ so that the velocity field is given by the integrals

$$\mathbf{u}(\mathbf{x}) = \int_\Sigma K_B^\delta(\mathbf{x} - \mathbf{y})\mathbf{f}(\mathbf{y})dS_y \quad \text{or} \quad \mathbf{u}(\mathbf{x}) = \int_\Gamma K_B^\delta(\mathbf{x} - \mathbf{x}(\ell))\mathbf{f}(\ell)d\ell,$$

respectively. For the presentation of a unified numerical method, we will use Eq. (5) for all cases under the assumption that each force $\mathbf{f}_k$ represents the force on the corresponding patch of surface area (e.g. $\mathbf{f}(\mathbf{y}_k)h^2$) or on a segment of the filament (e.g. $\mathbf{f}(\ell_k)h$), as necessary. This makes the method identical regardless of whether the formulation is a discretization of an integral or a superposition of individual forces at scattered points. Obviously, for specific cases of surface integrals one could modify the formulation to use more accurate quadrature rules and possibly fewer collocation points along the surfaces to increase the efficiency for that particular case, but we leave these details for another time.

Eq. (5) determines the velocity field at any location $\mathbf{x}$ given the surface forces $\mathbf{f}$. In cases when the velocity of a particle is known, the same equation can be used to compute the necessary forces. This is done by enforcing Eq. (5) at every point of the surface and solving the resulting linear system of equations. It is known that in some geometries, the integral operator that determines the matrix can give multiple solutions for the force. For example, a normal force of constant magnitude applied to the surface of a sphere will not cause any fluid motion due to the incompressibility (it will only increase the pressure inside), regardless of the magnitude of the force. This implies that in some cases, the matrix in Eq. (5) may be nearly singular. One can impose conditions such as zero average normal force to regain uniqueness. In the computations presented here, we have found that using the iterative procedure GMRES with zero initial guess works well without modifying the matrix.

2. The expressions for G_δ and B_δ

We consider here two ways of finding suitable functions G_δ and B_δ. The first attempt is based on removing the singularity of the known expressions from the previous section (for example, replacing $1/r$ with $1/\sqrt{r^2 + \delta^2}$). The expressions are readily found this way and, if desired, one can derive the formula for the corresponding blob ϕ_δ by differentiating G_δ. A different approach is to select a blob first and solve the corresponding ordinary differential equations for G_δ and B_δ. This is typically more challenging but it allows the use of blobs that satisfy specific moment conditions that might be required.

2.1. Selecting G_δ and B_δ by regularizing G and B

The simplest way to regularize the fluid velocity is to start with the expression for $B(r)$ from the singular case and modify it by setting

$$B_\delta(r) = \frac{1-e^{-\alpha R}}{4\pi\alpha^2 R}, \quad \text{with } R^2 = r^2+\delta^2.$$

This results in the corresponding functions

$$H_2(r) = -\frac{e^{-\alpha R}}{4\pi R^3}\left(\frac{3}{\alpha^2R^2}+\frac{3}{\alpha R}+1\right)+\frac{3}{4\pi\alpha^2R^5}$$

and

$$H_1(r) = \frac{e^{-\alpha R}}{4\pi R}\left(\frac{1}{\alpha^2R^2}+\frac{1}{\alpha R}+1\right)-\frac{1}{4\pi\alpha^2R^3}+\delta^2 H_2(r).$$

The corresponding regularized Green's function becomes

$$G_\delta(r) = -\frac{1}{4\pi R}-\delta^2 H_2(r).$$

We mention that this regularized Green's function corresponds to (i.e. ΔG_δ equals) the blob

$$\phi_\delta(r;\alpha) = \frac{3\delta^2}{4\pi R^5}-\delta^2\Delta H_2(r),$$

which depends on α due to the presence of $H_2(r)$. It is not difficult to show that this blob has the property that

$$4\pi\int_0^\infty r^2\ \phi_\delta(r;\alpha)dr = 1 \quad \text{independent of } \alpha$$

$$\lim_{\alpha\to 0}\phi_\delta(r;\alpha) = \frac{15\delta^4}{8\pi(r^2+\delta^2)^{7/2}}, \quad \lim_{\alpha\to\infty}\phi_\delta(r;\alpha) = \frac{3\delta^2}{4\pi(r^2+\delta^2)^{5/2}}.$$

Since there exists a blob (for each α) that produces the regularization, it is guaranteed that the regularized flow will retain the incompressibility property. This way of regularizing has the advantage that the velocity expression is trivially determined; on the other hand, the blob that corresponds to this regularization depends on α, which may not be desired. In addition, the blob results from the process instead of being chosen. This may be an issue if a blob is required to satisfy moment conditions or other constraints demanded by the method's accuracy.

2.2. Finding G_δ by first selecting the blob

The expression for G_δ given above has a feature that due to the δ^2 term, it depends on the physical parameter α even though this dependence is not there in the singular version. It would be difficult to guess a regularized version of $B(r)$ in such a way that once the corresponding G_δ is computed, it does not depend on α. Similarly, if a blob is required to satisfy certain conditions, one must first design the blob and then determine the regularized velocity formula that it produces. In Stokes flows, blobs are made to satisfy moment (or similar) conditions to improve the accuracy of the method [1,4]. This would necessitate starting with the blob and deriving the final expressions This can be accomplished if we begin with a blob and perform the necessary integration to derive B_δ.

Given any blob $\phi_\delta(r)$, the regularized Green's function satisfies

$$[rG_\delta(r)]'' = r\phi_\delta(r).$$

Integrating twice and using integration by parts, we get

$$rG_\delta(r) = rG_\delta(0)+r\int_0^r x\phi_\delta(x)dx-\int_0^r x^2\phi_\delta(x)dx.$$

Now, we use the assumption that the total integral of the blob is $4\pi\int_0^\infty x^2\phi_\delta(x)dx = 1$. We enforce the condition that $r\,G_\delta(r)\to -1/4\pi$ as $r\to\infty$ to get that

$$\lim_{r\to\infty} r\left(G_\delta(0)+\int_0^r x\phi_\delta(x)dx\right) = 0,$$

to arrive at

$$G_\delta(r) = -\int_0^\infty x\phi_\delta(x)dx+\frac{1}{r}\int_0^r (r-x)x\phi_\delta(x)dx. \tag{6}$$

Note that as $r\to\infty$, this function approaches $-1/4\pi r$.

In the next section, we will need the Laplace Transform of $r\,G_\delta(r)$ so we derive it here. If we denote $M_1 = \int_0^\infty x\phi_\delta(x)dx$, we get

$$rG_\delta(r) = -rM_1 + \int_0^r (r-x)x\phi_\delta(x)dx,$$

so that

$$\mathcal{L}[rG_\delta](s) = -\frac{M_1}{s^2} + \frac{\mathcal{L}[r\phi_\delta](s)}{s^2}.$$

We note that the singular $G(r)$ satisfies

$$G(r) = -\frac{1}{4\pi r}, \mathcal{L}[rG](s) = -\frac{1}{4\pi s}.$$

2.2.1. Solving for B_δ

We first look at Eq. (3). if we define $Y(r) = rB_\delta$, we can write the equation as

$$Y''(r) - \alpha^2 Y(r) = rG_\delta(r). \tag{7}$$

Note that $Y(0) = 0$ and $Y'(0) = B_\delta(0)$ since $B_\delta(r)$ is smooth. We take Laplace Transforms of the differential equation to get

$$(s^2 - \alpha^2)\widehat{Y}(s) - B_\delta(0) = \mathcal{L}[rG_\delta](s) = -\frac{M_1}{s^2} + \frac{\mathcal{L}[r\phi_\delta](s)}{s^2}.$$

Solving for $\widehat{Y}(s)$ and finding the inverse Laplace transform we get

$$Y(r) = \frac{B_\delta(0)}{\alpha}\sinh(\alpha r) + \frac{M_1}{\alpha^2}r - \frac{M_1}{\alpha^3}\sinh(\alpha r) + \frac{1}{\alpha^3}\int_0^r [\sinh(\alpha(r-x)) - \alpha(r-x)]x\phi_\delta(x)dx.$$

Now we divide by r to find

$$B_\delta(r) = \left[B_\delta(0) - \frac{M_1}{\alpha^2}\right]\frac{\sinh(\alpha r)}{\alpha r} + \frac{M_1}{\alpha^2} + \frac{1}{\alpha^3 r}\int_0^r [\sinh(\alpha(r-x)) - \alpha(r-x)]x\phi_\delta(x)dx.$$

The constant $B_\delta(0)$ can be computed by isolating the coefficient of the growing exponential $e^{\alpha r}$ and setting it to zero. This gives

$$B_\delta(0) = \frac{M_1}{\alpha^2} - \frac{1}{\alpha^2}\int_0^\infty e^{-\alpha x}x\phi_\delta(x)dx.$$

We finally get that for Brinkman flows

$$B_\delta(r) = \frac{1}{\alpha^2}\int_0^\infty \left[1 - e^{-\alpha x}\frac{\sinh(\alpha r)}{\alpha r}\right]x\phi_\delta(x)dx + \frac{1}{\alpha^3 r}\int_0^r [\sinh(\alpha(r-x)) - \alpha(r-x)]x\phi_\delta(x)dx. \tag{8}$$

2.2.2. The limit of $B_\delta(r)$ as $\delta \to 0$

The expression for $B(r)$ without regularization is known to be

$$B(r) = \frac{1 - e^{-\alpha r}}{4\pi\alpha^2 r}$$

and one can verify that the series expansion of Eq. (8) for small δ gives

$$B_\delta(r) = \frac{1 - e^{-\alpha r}}{4\pi\alpha^2 r} + O(\delta).$$

2.2.3. The full formulas for a specific blob

In order to develop the regularized expressions based on a blob that does not depend on the physical parameters of the problem, we begin by choosing a blob and using Eq. (8) to find the corresponding B_δ. The only limitation in this process is our ability to find the associated integrals in Eq. (8). Here we consider a blob with exponential decay and $\phi'_\delta(0) = 0$ (for symmetry)

$$\phi_\delta(r) = \frac{(r+2\delta)^2}{224\pi\delta^5}e^{-r/\delta}$$

whose exponential form allows the analytical computation of the integrals related to B_δ. The required properties of $\phi_\delta(r)$ are that its total volume integral be 1, that it be smooth and decay sufficiently fast as $r \to \infty$. Notice that we can write the blob as a function of $z = r/\delta$

$$\phi_\delta(z) = \frac{(z+2)^2}{224\pi\delta^3}e^{-z}.$$

We will use this form to simplify the notation. To find the regularized Green's function, we solve

$$rG_\delta'' + 2G_\delta' = r\phi_\delta(r),$$

which gives

$$G_\delta(z) = \frac{(z+4)(z^2+6z+14)e^{-z} - 56}{224\pi\delta z}.$$

Note that G_δ is regular at the origin since a series expansion about $z = 0$ yields

$$G_\delta(z) = -\frac{9}{112\pi\delta} + O(z^2).$$

The next step is to find B_δ by substituting the Green's function into Eq. (1), or equivalently, plug $\phi_\delta(r)$ into Eq. (8). This gives

$$B_\delta(z) = \frac{1}{4\pi\sigma\alpha}\frac{(1-e^{-z})}{z} + \frac{(\sigma^2-7)}{28\pi\sigma\alpha(\sigma^2-1)^4}\frac{(e^{-\sigma z}-e^{-z})}{z} - \frac{\sigma e^{-z}}{224\pi\alpha(\sigma^2-1)}\left[z^2 + \frac{2(5\sigma^2-8)}{(\sigma^2-1)}z + \frac{2(19\sigma^4-55\sigma^2+48)}{(\sigma^2-1)^2}\right],$$

where $\sigma = \alpha\delta$.

Returning to the coordinate $r = \delta z$ and noting that $\sigma z = \alpha r$, we can write

$$B_\delta(r) = \frac{1}{4\pi\alpha^2}\frac{(1-e^{-r/\delta})}{r} + \frac{(\alpha^2\delta^2-7)}{28\pi\alpha^2(\alpha^2\delta^2-1)^4}\frac{\left(e^{-\alpha r}-e^{-r/\delta}\right)}{r} - \frac{\delta e^{-r/\delta}}{224\pi(\alpha^2\delta^2-1)}\left[r^2/\delta^2 + \frac{2(5\alpha^2\delta^2-8)}{(\alpha^2\delta^2-1)}r/\delta + \frac{2(19\alpha^4\delta^4-55\alpha^2\delta^2+48)}{(\alpha^2\delta^2-1)^2}\right],$$

where one can see that for fixed α and r,

$$\lim_{\delta\to 0} B_\delta(r) = \frac{1-e^{-\alpha r}}{4\pi\alpha^2 r}.$$

From the above expression for $B_\delta(r)$ one can easily derive the corresponding $H_1(r)$ and $H_2(r)$.

3. Numerical examples

We present first two validation studies to provide insight into the effect of the numerical parameters on the results. The first problem is to compute the drag on a solid sphere translating in a Brinkman flow. The second validation study is for flow in a channel of circular cross-section. Two applications to biological flows complete the section, including the connection between Brinkman flows and oscillatory unsteady Stokes flows.

3.1. Sphere in a uniform Brinkman flow

A first test case is a stationary sphere in a uniform Brinkman flow. We aim to compare the disturbance flow around the sphere using the numerical method presented here and the two regularizations described in the previous section. We consider a sphere of radius a and discretize its surface using Spherical Centroid Voronoi Tessellation (SCVT) and the package STRIPACK [5,17]. Using SCVT, a specified number of points are positioned on a unit sphere so that the points are well separated. Then, the Delaunay triangulation of these same points on the unit sphere is obtained using STRIPACK. We then use the centroid of each triangle as the location of the N point forces, $\mathbf{f}_i\phi_\delta$, where $i = 1,2\ldots N$. The velocity of all points on the surface of the sphere is set to a constant vector $\mathbf{U}$ and we use Eq. (4) to solve for the forces. For α, we use the five values $\alpha = 0.1$, 1, 5, 10, 20 and choose δ based on the discretization.

As in the case of a sphere in Stokes flow, the velocity field outside the sphere in a Brinkman flow can be found exactly by combining a Brinkmanlet and a dipole with the appropriate strength located at the center of the sphere. The strength of the Brinkmanlet is $\mathbf{f} = 6\pi\mu a\, e^{\alpha a}\mathbf{U}$ and the corresponding dipole strength is the one that produces a uniform velocity on the sphere. The traction at a point $\mathbf{x}$ on the surface of the sphere is [14]

$$\mathbf{f}(\mathbf{x}) = -\frac{3\mu}{2a}\left((1+a\alpha)\mathbf{U} + \frac{a^2\alpha^2}{3}(\mathbf{U}\cdot\hat{n})\hat{n}\right),$$

where $\hat{n}$ is the unit vector normal to the sphere. This expression becomes uniform only for the case $\alpha = 0$, as it is known for Stokes flows. For $\alpha > 0$, the traction varies along the surface of the sphere. The drag on the sphere is given by the well-known formula [2],

$$F_{drag}(\alpha) = 6\pi\mu a|\mathbf{U}|\left(1+\alpha+\alpha^2/3\right).$$

We note here that a stationary sphere in a non-zero uniform Brinkman flow differs from a translating sphere in an otherwise zero flow due to the fact that, at infinity, the lower-order resistance term in the Brinkman equation is non-zero when the

sphere is stationary and zero when the sphere is translating, thus the pressure induces a greater overall force on the sphere in the former case.

Fig. 1 shows the streamlines around the sphere for a uniform upward flow in the cases $\alpha = 0.1$ (small departure from Stokes flow) and $\alpha = 100$. Notice that the disturbance due to the sphere decays faster for larger α, which is also shown in [19]. For various fixed values of α, we computed the drag force on the stationary sphere using our regularization method. Given a discretization of the sphere with N points, the formula in Eq. (5) evaluated at the same surface points was solved as a linear system for the forces $\mathbf{f}_k$ provided the velocities at all points were equal. The forces were then summed to compute the drag and the results listed in Table 1.

The results have been optimized in the sense that for each value of α we have chosen the value of δ that minimizes the error in the drag of the sphere. This results in the empirical relation $\delta_2 = 0.212\delta_1$ (where δ_1 corresponds to Reg 1 and δ_2 corresponds to Reg 2). This can be explained by realizing that the two blobs have very different decay rates. The blob of Section 2.1 (Reg 1) depends on α so its shape changes with the permeability; however, we showed that this blob has algebraic decay ranging from r^{-7} to r^{-5}. On the other hand, the blob from Section 2.2 (Reg 2) has exponential decay $e^{-r/\delta}$ independently of α. A fair way to compare the performance of the two regularizations is to scale them differently so that the two blobs agree at $r = 0$ (see Fig. 2). This results in $\delta_2 = 0.212\delta_1$.

We also consider the speed of the flow along a horizontal line through the center of the stationary sphere. In Fig. 3, we plot the vertical velocity component from the edge of the sphere out to one unit away from the edge of the sphere. The figure shows three curves for five different values of α: the exact solution (see [15,8]), the numerical solution with the regularization in Section 2.1, and the numerical solution with the regularization in Section 2.2. The comparison shows that both blobs perform very well for a large range of α values although the results are better when the fluid velocity near the surface of the sphere does not surpass the uniform flow at infinity.

3.2. A rotating sphere in a quiescent Brinkman flow

We now consider the fluid motion generated when we rotate the sphere with a constant angular velocity Ω without any additional background flow. Its surface develops tangential forces so that the flow outside the sphere along a line segment emanating from the surface of the sphere and perpendicular to the direction of the angular velocity is given by [20]

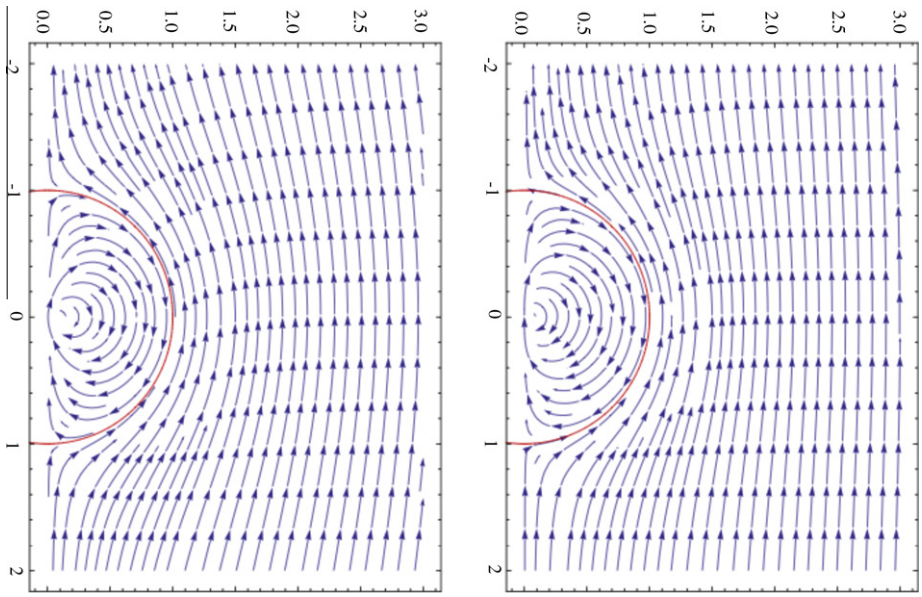

Fig. 1. Streamlines around the sphere for $\alpha = 0.1$ (left) and $\alpha = 100$ (right). The sphere has radius $a = 1$.

Table 1
Computed values of the drag on a sphere translating in a Brinkman flow. The number of triangles acquired with SCVT and STRIPACK in all computations was $N = 7996$.

α	δ-Reg 1	δ-Reg 2	F_{drag}-Reg 1	F_{drag}-Reg 2	F_{drag} Exact
0.1	0.016	0.0034	20.8019	20.7957	20.7973
1	0.018	0.0038	44.0059	43.9757	43.9823
5	0.029	0.0062	270.0281	269.7660	270.1770
10	0.0373	0.00815	835.7700	835.5633	835.6636
20	0.0454	0.0102	2909.2852	2910.1664	2909.1147

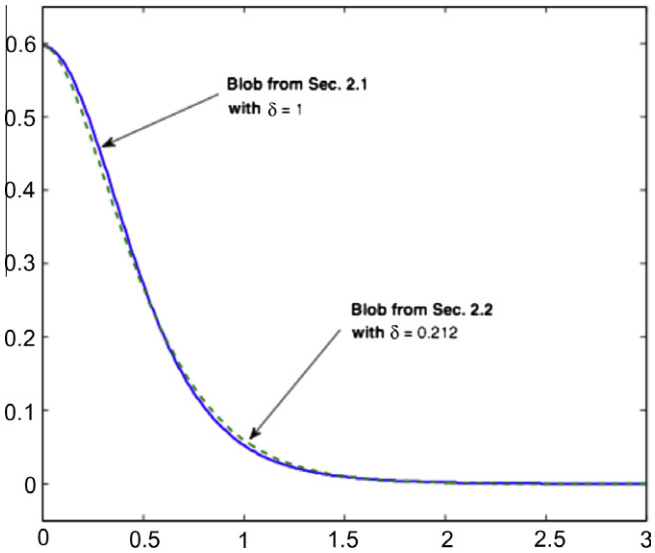

Fig. 2. Plots of $\phi_\delta(r)$ for the two different regularizations and $\alpha = 0$. The comparison is made using different values of δ so that the functions agree at $r = 0$. If δ_1 is the regularization parameter used in the blob of Section 2.1 and δ_2 the regularization parameter used in the blob of Section 2.2, the result is $\delta_2 = 0.212\delta_1$. Note that the shapes are not significantly different.

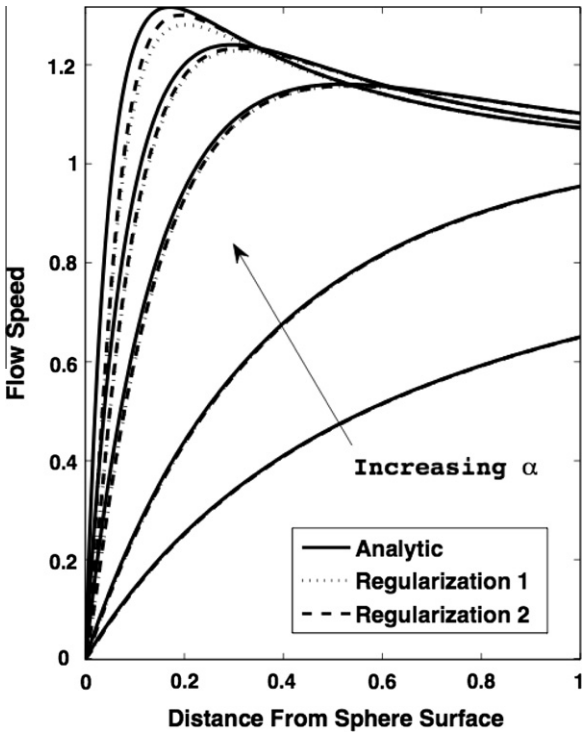

Fig. 3. Vertical velocity component along a sphere centerline perpendicular to the flow direction. The sphere radius is $a = 1$. The graph shows three curves for each of the values of $\alpha = 0.1, 1, 5, 10, 20$. The three curves correspond to the exact solution (solid), the numerical solution with the regularization in Section 2.1 (dotted), and the numerical solution with the regularization in Section 2.2 (dashed).

$$\mathbf{u}(\mathbf{x}) = \boldsymbol{\Omega} \times \mathbf{x} f(r) \quad \text{with } f(r) = e^{\alpha(1-r/a)} \frac{a^3(1+\alpha r/a)}{r^3(1+\alpha)}.$$

The factor $f(r)$ in this velocity field for several values of α is shown in Fig. 4. The regularization parameters were fixed at $\delta = 0.014$ and $\delta = 0.003$ for the regularizations from Sections 2.1 and 2.2, respectively. The numerical results show excellent

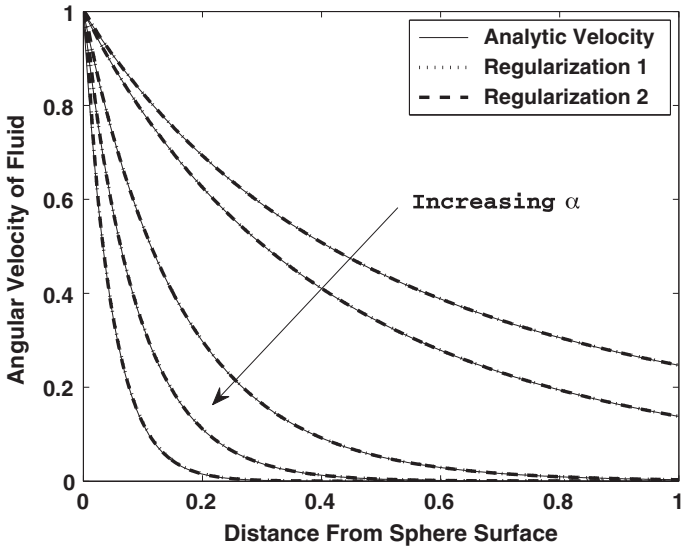

Fig. 4. Plot of $f(r)$ in the velocity field $\mathbf{u}(\mathbf{x}) = \boldsymbol{\Omega} \times \mathbf{x} f(r)$ outside a rotating sphere along a line through the center of the sphere. The angular velocity $\boldsymbol{\Omega} = (0,0,1)$. The sphere radius is $a = 1$. The graph shows two curves for each of the values of $\alpha = 0.1, 1, 5, 10, 20$. Besides the analytic solution, the two curves correspond to the numerical solutions with the regularization in Section 2.1 (dotted), and the numerical solution with the regularization in Section 2.2 (dashed).

agreement with the theory. The net torque can be computed by applying the angular velocity to the points on the sphere and solving for the forces as before. The torques are then computed simply as $\sum_k \mathbf{x}_k \times \mathbf{f}_k$ and compared with the formula [20]

$$T(\alpha) = 8\pi a^3 |\boldsymbol{\Omega}| \frac{1 + \alpha + \alpha^2/3}{1 + \alpha}.$$

Our computations show that the computed net torque is sensitive to the regularization parameter δ. For the fixed values used in Fig. 4, $\delta = 0.014$ for regularization 1 and $\delta = 0.003$ for regularization 2, the net torque is overestimated by the method using either regularizing function. On the other hand, by decreasing the values of δ as α increases, the net torque approximation can be made to match the exact value, as summarized in Table 2.

3.3. Brinkman flow in a cylindrical channel

As a second validation test we consider a cylindrical channel with circular cross-section of radius a and length L, and we impose an internal flow, U, and hold the cylinder fixed. The channel is long enough such that the inlet flow has fully developed by the time it reaches the center of the cylinder and is not affected by the outlet. The axial velocity component in the channel as a function of r can be compared with the explicit formula [21]

$$U(r,\alpha) = U_0 \frac{I_0(a\alpha)}{I_2(a\alpha)} \left[1 - \frac{I_0(r\alpha)}{I_0(a\alpha)}\right],$$

where U_0 is the average velocity of the fluid in the channel and I_k is the Bessel function of the second kind of order k.

Fig. 5 shows the axial velocity component inside the cylinder along the center line of a cross-section. The computations were done using a channel of length $L = 4$ and radius $a = 1$ whose surface is discretized using a cylindrical grid of 92 equally-distributed cross-sections with 144 equally-spaced points around the circumference of each cross-section.

The regularization parameter used to create the plots in this Figure was $\delta = 0.014$ for the blob in Section 2.1 and $\delta = 0.003$ for the blob in Section 2.2. To achieve the approximate axial velocity for this problem, there was a range of values of δ that

Table 2
Computed values of the net torque on a sphere rotating in a Brinkman flow. The number of triangles acquired with SCVT and STRIPACK in all computations was $N = 7996$.

α	δ-Reg 1	δ-Reg 2	Torque-Reg 1	Torque-Reg 2	Torque exact
0.1	0.01400	0.003000	25.25	25.24	25.20
1	0.00550	0.001200	29.43	29.47	29.32
5	0.00240	0.000510	60.11	59.92	60.039
10	0.00300	0.000640	101.66	101.42	101.29
20	0.00425	0.000915	184.15	184.61	184.70

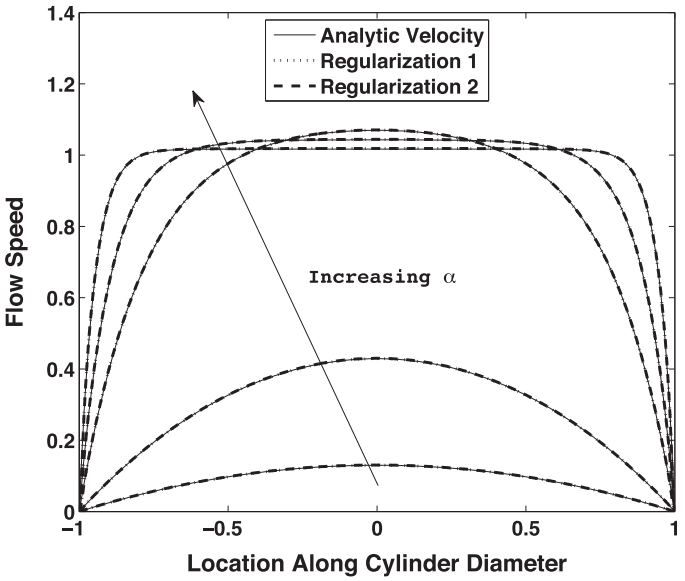

Fig. 5. Axial velocity inside the cyliner of radius $a = 1$. The graph shows three curves for each of the values of $\alpha = 0.1$, 1, 2, 5, 100. The three curves correspond to the exact solution (solid), the numerical solution with the regularization in Section 2.1 (dotted), and the numerical solution with the regularization in Section 2.2 (dashed).

seemed to work. The computed velocities began to diverge from the exact ones for values above $\delta = 0.02$ for the blob in Section 2.1 and $\delta = 0.004$ for the blob in Section 2.2. Notice that the values of δ that achieved good results are at the low end of what was used in the example using a stationary sphere in a Brinkman flow, and do not change with α.

3.4. Undulating organism swimming in a Brinkman fluid

As an application, we consider an organism defined by a curve in three-dimensional space. Forces along the organism develop in such a way to make it undulate by passing a wave from front to back, propelling the organism. The goal here is to determine the effect of the permeability parameter α on the swimming speed of the organism.

The organism is defined initially by the parametric equations $x(s) = s$, $y(s) = A(s)\sin(m\,s)$, and $z(s) = 0$ for $0 \leqslant s \leqslant L$ and $m = 2\pi/L$ where all quantities are dimensionless. We choose the amplitude $A(s)$ to be a linearly increasing function. In order to generate forces along the curve, we imagine an ideal "target" shape given by $Y(s,t) = A(s)\sin(m(s-t))$ and so that the forces will develop in order to maintain approximately the total length of the curve and the curvature corresponding to $Y(s,t)$. Let there be N equally-distributed points along the organism separated by a distance $h = L/(N-1)$. We first define an energy by

$$\mathcal{E} = \sum_{k=1}^{N-1} \sigma_s \left(\frac{|\mathbf{x}_{k+1} - \mathbf{x}_k|}{h} - 1 \right)^2 + \sum_{k=2}^{N-1} \sigma_b \left(\frac{(\mathbf{x}_{k+1} - \mathbf{x}_k) \times (\mathbf{x}_k - \mathbf{x}_{k-1})}{h^3} - \kappa_k \right)^2,$$

where the first sum represents the spring energy due to stretching and the second sum is the bending energy due to a mismatch of the computed curvature and the target curvature κ_k of $Y(s,t)$ at $s = kh$. The force at (x_k, y_k, z_k) is defined as

$$\mathbf{f}_k(t) = -\partial\mathcal{E}/\partial\mathbf{x}_k,$$

which ensures that the total force on the organism is zero so that the forward motion is not due to a net external force. We emphasize that this formulation does not enforce the position of the organism, only its shape. Its location and orientation are free to change.

In this example, the dimensionless parameters $\sigma_s = 100$ and $\sigma_b = 0.05$ are fixed for all time and the velocity of the points defining the organism is computed using Eq. (4). A typical motion of the organism over a single period of time is shown in Fig. 6. The parameters used in $Y(s,t) = A(s)\sin(m(s-t))$ were $L = 0.75$, $m = 2\pi/L$, $A(s) = 5$ s/m^2. The point separation along the organism was approximately $h = L/(N-1)$ and the regularization parameter was set to $\delta = 0.25$ h. Fig. 6 shows the organism at equal intervals of dimensionless time over one period $0 \leqslant s \leqslant 0.75$. In our simulations, the virtual organism propels itself at a constant speed and requires approximately 80 periods to swim one body length.

Based on the initial and final location of the front point, we compute an average swimming speed for every value of α. The results are shown in Fig. 7.

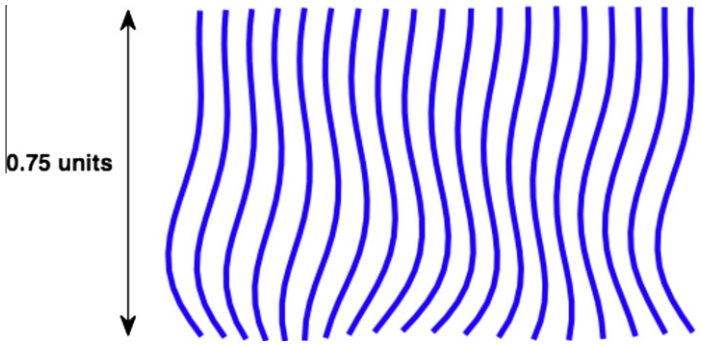

Fig. 6. Organism shape during one period of swimming with $\alpha = 10$. The figures are plotted on a 1:1 scale. The leftmost figure is the initial shape; the other figures are the shapes at equally distributed time intervals displaced to the right for viewing. The swimming motion is upward although difficult to perceive over a single period.

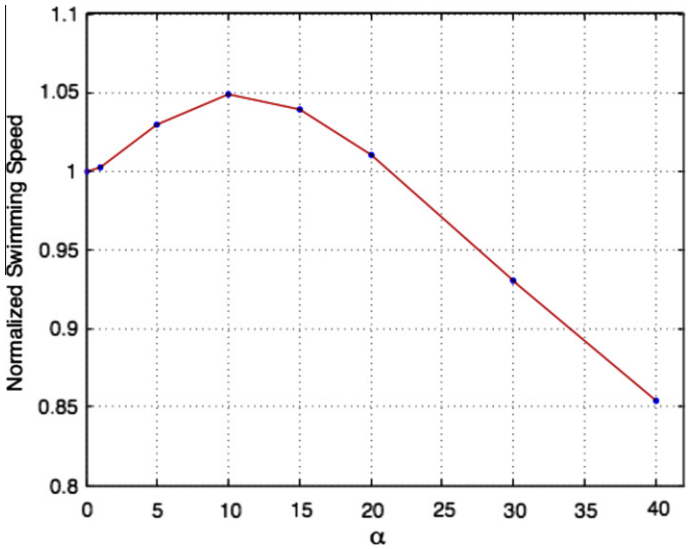

Fig. 7. Organism swimming speed as a function of α scaled by the swimming speed in Stokes flow ($\alpha = 0$).

As α increases, the swimming speed is initially enhanced compared to the Stokes case until a point of maximum propulsion around $\alpha = 10$. For even larger values of α the swimming speed begins to decrease, indicating that the permeability of the medium is too low for the organism to make its way through it. This phenomenon of higher swimming speed in a Brinkman flow compared to Stokes flows has been observed before. In the context of a swimming sheet, asymptotic analysis in [13] for small wave amplitude shows that, to leading order, the propulsion speed (relative to Stokes flow) is $U(\alpha) = U(0)\sqrt{1 + \alpha^2/(m^2L^2)}$.

3.5. Application to oscillatory unsteady Stokes

The unsteady Stokes equations for incompressible flow are

$$\rho\frac{\partial \mathbf{u}}{\partial t} = -\nabla p + \mu\Delta\mathbf{u} + \mathbf{F}, \nabla\cdot\mathbf{u} = 0 \tag{9}$$

where ρ is the fluid density. As before, we assume that $\mathbf{F}$ is given by a single regularized force centered at the origin $\mathbf{F}(t,\mathbf{x}) = \mathbf{f}(t)\phi_\delta(\mathbf{x})$ and that the flow is oscillatory. Then we can write

$$\mathbf{u}(t,\mathbf{x}) = e^{i\omega t}\mathbf{u}(\mathbf{x}), p(t,\mathbf{x}) = e^{i\omega t}p(\mathbf{x}), \mathbf{f}(t) = e^{i\omega t}\mathbf{f}.$$

After plugging this into the equations, we get

$$(\mu\Delta - i\omega\rho I)\mathbf{u}(\mathbf{x}) = \nabla p(\mathbf{x}) - \mathbf{f}\ \phi_\delta(\mathbf{x}), \nabla\cdot\mathbf{u} = 0. \tag{10}$$

Writing these equations in dimensionless form and setting $\alpha^2 = iL^2\omega\rho/\mu$, we find that the unsteady Stokes equations for oscillatory flows reduces exactly to the Brinkman equation so that the velocity field is given by Eq. (4). The only difference is that the parameter α^2 is now imaginary. However, the computational simulations are done in exactly the same way as before.

We apply this method to the feeding appendage oscillations of the planktonic crustacean *Eucalanus pileatus* (Fig. 8(a)). Copepods such as *E. pileatus* are only a few millimeters long and have appendages ending in arrays of long, thin bristles called setae. Many of these appendages are used in the feeding process, including the first and second maxillae (M1 and M2 in Fig. 8(a)). There was a long-standing debate over whether these organisms used their bristled appendages as "rakes" to sieve food out of the water, or whether the bristles acted more like "paddles" that direct food particles toward the mouth using currents. Cheer and Koehl [3] used a steady Stokes flow model to demonstrate that the bristles can undergo a functional shift between paddle and rake by changing the speed or separation of the setae. Using the Brinkman regularization method on a linear array of setae, we may assess the functional shift in the case of oscillatory flow.

In particular, we will look at the activity of the feeding appendages called the second maxillae (Fig. 8(a)). When *E. pileatus* feeds on small food cells ($\approx$6 μm), the second maxillae exhibit low amplitude oscillatory motion at about 20 Hz interrupted by occasional "combing" actions [16]. No absolute velocities for the second maxillae are available for this feeding regime, so we take the peak velocity to be 7 mm/s, the maximum velocity observed for the second maxillae during no capture motions in the presence of large food cells ($\approx 30 - 40$ μm) [12]. For the purposes of this example, we assume that the diameter of the setae, d, on the second maxillae is 10 μm [3] and that the setae have a length of $L = 250$ μm based on images in Koehl [11] and Koehl and Strickler [12]. Koehl and Strickler report maximum separations between setae from $30 - 50$ μm, so we assume basal separations of 20 μm and tip separations varying from $20 - 50$ μm as in the schematic in Fig. 8(b). For this example, we do not consider the flow field caused by the body of the copepod; instead, we consider only the flow between four setae of equal length. One could account for the effect of the body by using a method of images, but that is not needed to compare to Cheer and Koehl [3].

We discretize the four setae into L/d points and take the blob parameter δ to be $d/5$. The velocity at each of these points is fixed at 7 mm/s, and the force distributions $\mathbf{f}(\mathbf{x})$ along the setae required to maintain this velocity are calculated from the inverse of Eq. (4), where H_1 and H_2 are computed from the unsteady Stokes equations and the regularization in Section 2.2. The forces $\mathbf{f}(\mathbf{x})$ are used in Eq. (4) to calculate the fluid velocity field between the setae.

Fig. 9 shows the peak velocity and phase shift profiles for the fluid parcels midway between the two innermost of four setae with various amounts of setae tip separation. The ordinate is distance along a seta in microns, and the abscissa is either peak velocity in mm/s (Fig. 9(a)) or phase shift in degrees (Fig. 9(b)). The legend denotes tip separation in microns. As tip separation increases, the fluid between the setae moves more slowly and lags farther behind the setae. Near the mid-point

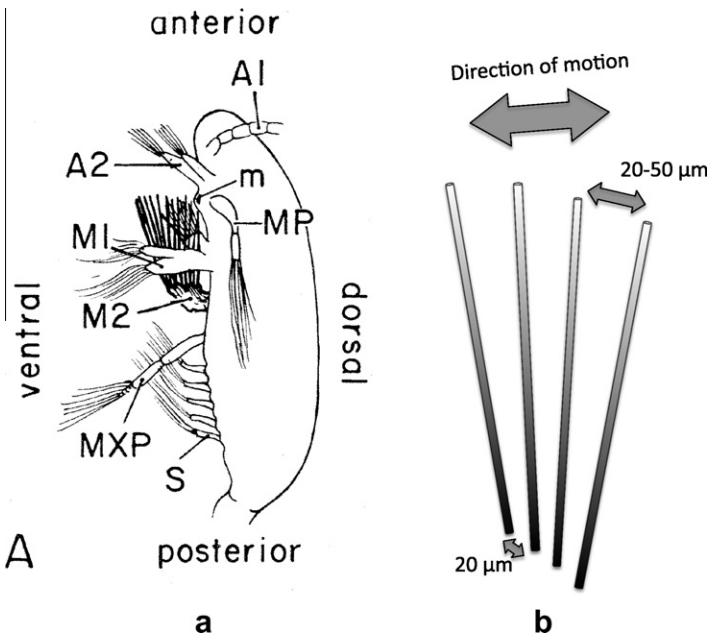

Fig. 8. (a) A diagram of *Eucalanus pileatus* in a typical feeding posture viewed from the left side. The feeding appendages are: A2 – second antenna, M1 – first maxilla, M2 – second maxilla, MP – mandibular palp, and MXP – maxilliped. Other structures are: *m* – mouth, A1 – first antenna, and *S* – swimming legs. This figure was reproduced with permission from [12]– copyright (1981) by the American Society of Limnology and Oceanography, Inc. (b) A schematic of the numerical simulation: four setae of identical length moving sinusoidally through seawater. The direction of motion is perpendicular to the long axis of the setae and to the axis connecting all four setae. The setae may be splayed near their tips.

of the setae, peak fluid velocity ranges from about 5.75 − 6.25 mm/s, or 80 − 90% of the velocity of the setae themselves. This suggests that a significant amount of fluid is being dragged along with the setae during their total excursion.

Cheer and Koehl [3] quantified the amount of fluid carried between two steadily moving cylindrical hairs or bristles by constructing a "leakiness" ratio. Using a steady Stokes model of two-dimensional fluid motion between cylinders, they calculated the ratio of actual fluid flow between the cylinders to the volume swept out by the pair over one unit of time. When the leakiness is near zero, then the pair of cylinders acts more like a solid paddle than sieve or a rake due to the mass of fluid dragged along with the setae. When the leakiness is near one, then the opposite scenario holds and the bristles are functionally equivalent to sieves. Cheer and Koehl showed that changing the separation between the bristles and/or the velocity of the bristles can cause a functional shift between paddle and rake.

We can calculate the same ratio for the setae array in Fig. 8, where the volume considered is that between all four setae and the unit of time is half of one period of an oscillation. Fig. 10 graphs the leakiness that we calculated from our simulations of the motion of four setae moving at frequencies of 20–80 Hz. These frequencies are in the range reported for the

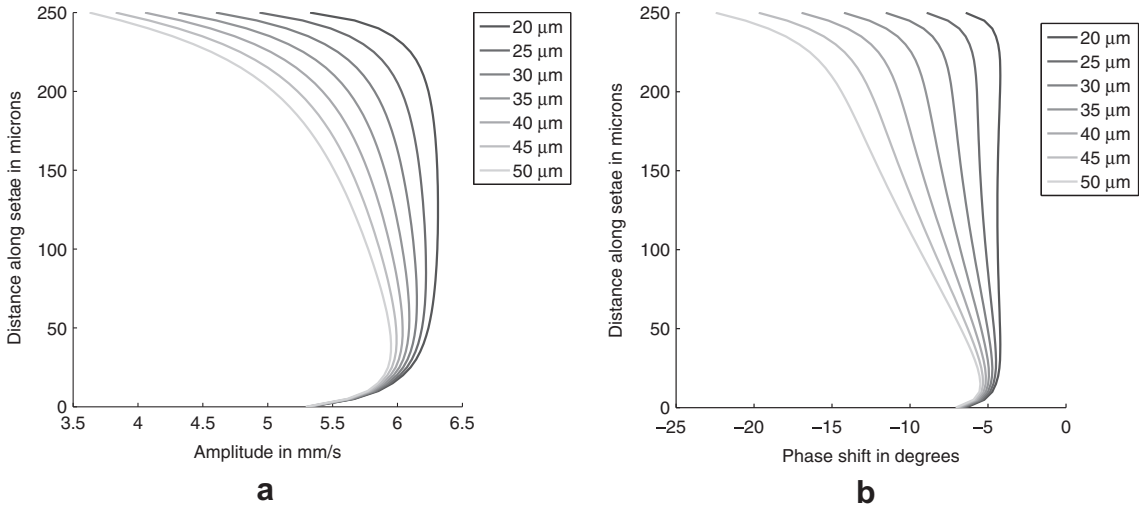

Fig. 9. The velocity (a) and phase (b) profiles for the fluid midway between the innermost setae in Fig. 8 when all the setae are moving sinusoidally at 20 Hz with a peak velocity of 7 mm/s. The ordinate represents distance along the setae, so that the profiles are vertical traces of the peak velocity in mm/s and phase shift in degrees. The legend gives the setae tip separation in microns.

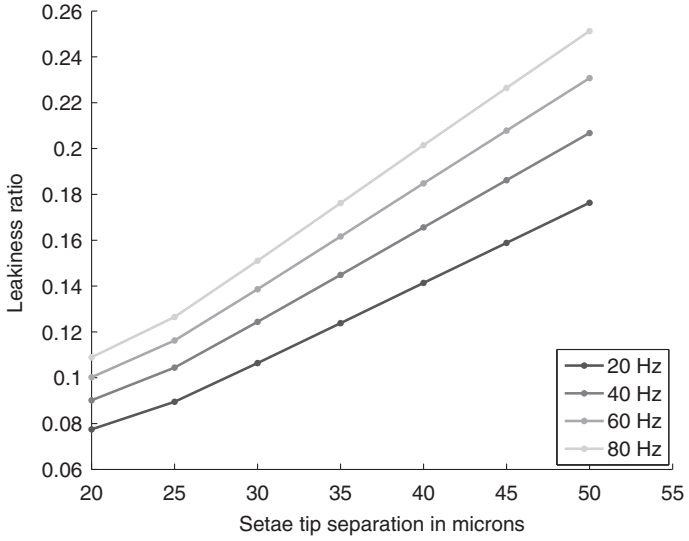

Fig. 10. Leakiness ratio versus tip separation for four simulated setae. A leakiness of zero means that the setae act as a solid paddle (all of the fluid between them moves at the same speed as the setae). A leakiness of one means that the setae act as a sieve (no fluid is pulled along with the setae motion). The simulated setae have a peak velocity of 7 mm/s, have 10 μm diameters, and are separated at the base by 20 μm. The abscissa is tip separation in microns.

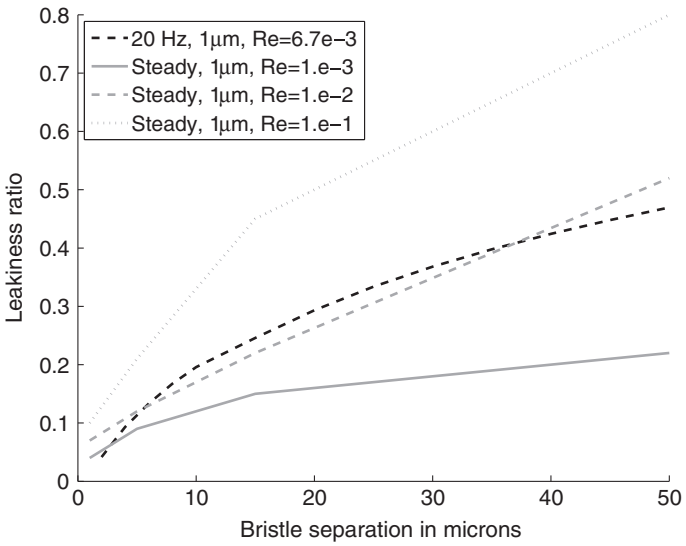

Fig. 11. Leakiness ratio versus setae separation using a scenario from Cheer and Koehl [3]. The gray lines represent calculations reconstructed from Fig. 5(a) in Cheer and Koehl for two bristles with 1 μm diameters moving at steady speeds that produce Reynolds numbers of 1.e-3, 1.e-2, and 1.e-1. These bristles are separated by a uniform spacing from base to tip (abscissa, in microns). The black dashed line is our calculation for two bristles with 1 μm diameters moving sinusoidally at 20 Hz and 7 mm/s, corresponding to a Reynolds number of approximately 6.7e-3. As in Cheer and Koehl, these bristles are also uniformly separated.

feeding appendage motion of several species of copepod [12,16]. This figure demonstrates that setae in this configuration are paddle-like in their function, although leakiness increases with both frequency and setae separation. This suggests that copepod appendages can shift their functionality not only by changing their speed and bristle separation, but also by changing their frequency of motion.

In order to directly compare our results for sinusoidal flow to the steady flow results from Cheer and Koehl, we repeated their simulations using the Brinkman regularization. Imposing a bristle motion of 20 Hz at 7 mm/s, we calculated the leakiness for two 165 μm bristles of 1 μm diameter that are uniformly separated rather than splayed as in our previous simulation. The results are given by the black dashed line in Fig. 11. This scenario is characterized by a Reynolds number of approximately 6.7e-3. For comparison, the results from Cheer and Koehl for bristles of 1 μm diameter at Reynolds numbers of 1.e-3–1.e-1 are shown in gray. If sinusoidal motion produces leakiness quantitatively similar to steady motion, then the black dashed line should fall between the solid and dashed gray lines. However, the sinusoidal motion shows more leakiness than predicted by steady flow for the given Reynolds number. This could be due to the sinusoidal motion or to fluid escaping over the top and bottom of the bristle array, which it cannot in Cheer and Koehl's model. The latter hypothesis is supported by the fact that shorter bristles show even more leakiness than the black dashed line in Fig. 11 for the same parameter choices (data not shown).

The row of four thicker, splayed bristles moving at 20 Hz in Fig. 10 (black line) shows more paddle-like behavior than the two thin, uniformly separated bristles in Fig. 11 (black dashed line). This is most likely due to the smaller volume between the bristles in the splayed array and the greater number of bristles in the array, since a longer array means that it is harder for fluid to escape around the sides. The exploration of these alternative geometries is facilitated by the Brinkman regularization.

4. Conclusions

We have introduced a regularization method for the numerical solution of the Brinkman equations for flows generated by external forces. The key feature of the method is to apply forces of the form $\mathbf{f}\phi_\delta(|\mathbf{x}-\mathbf{x}_0|)$ so that they are localized but smoothly transitioning from a maximum value at $\mathbf{x}_0$ to zero when $|\mathbf{x}-\mathbf{x}_0| \gg \delta$. For this type of forcing with N forces, the exact solution of the Brinkman equations can be found by the representation formula

$$\mathbf{u}(\mathbf{x}) = \sum_{k=1}^{N} K_B^\delta(\mathbf{x}-\mathbf{x}_k)\mathbf{f}_k = \sum_{k=1}^{N} \mathbf{f}_k H_1(|\mathbf{x}-\mathbf{x}_k|) + [\mathbf{f}_k \cdot (\mathbf{x}-\mathbf{x}_0)](\mathbf{x}-\mathbf{x}_0)H_2(|\mathbf{x}-\mathbf{x}_0|).$$

This formula may represent the superposition of flows generated by a collection of N forces exerted at scattered points, or the discretization of a surface or line integral with a force field along them. The validation studies of flows around a translating or rotating sphere and the flow inside a cylinder show that the method gives results that agree well with theory. Currently, there is no convergence theory for the method to provide guidance on how to choose the numerical parameter δ as a function

of the discretization of a surface or filament. In addition, in the case of surface discretizations, one could modify the quadrature rule to improve the accuracy; this will alter the relationship between the optimal δ and the discretization. In the simulation of a rotating sphere, the regularization parameters had to be chosen smaller than for the translating sphere. This implies that in order to get good agreement in both translation and rotation, the sphere surface discretization must be fine enough to allow the small values of δ required by the torque computation while making sure the surface grid is fine enough to prevent fluid leaking through it.

The method gives particularly good results for relatively large permeability (small α), which corresponds to the scale in which the Brinkman equations are valid. If $\alpha = 0$ the equation reduces to the Stokes equation and the method reduces to the method of regularized Stokeslets [4], which has been used widely in problems of microorganism motility. Our results show that if an undulating microorganism moves in a Brinkman fluid, its average swimming speed depends on α and that the maximum speed occurs at a nonzero value of α. This enhanced propulsion due to permeability has been observed before. In [13], the author shows this effect using a weakly nonlinear analysis on a swimming sheet and through numerical computations of a helical filament.

We have used the same methodology to model the flow due to an oscillating filament in unsteady Stokes flow. When the oscillation is explicitly introduced into the time-dependence of the variables, the resulting equation is the Brinkman equation with imaginary α^2. The method proceeds as before with the exception that the kernel $K_B(r)$ is separated into its real and imaginary parts. Any increase in computational cost in this application is due to the use of complex arithmetic throughout the simulation. We have applied the method to the feeding appendage oscillations of a copepod. The leakiness ratio, first computed in [3], is used to determine the conditions under which the appendages function as paddles or rakes. Our results suggest that copepod appendages can shift their functionality not only by changing their speed and bristle separation, but also by changing their frequency of motion.

Finally, the same approach can be used in two dimension flows, where the velocity expression is

$$\mathbf{u}(\mathbf{x}) = \mathbf{f}\, H_1(r) + (\mathbf{f}\cdot\mathbf{x})\mathbf{x}\, H_2(r)$$

with

$$H_1(r) = -B'', \quad H_2(r) = \frac{rB'' - B'}{r^3}$$

and the function $B(r)$ is given in terms of a modified Bessel function of the second kind [22]

$$B(r) = \frac{1}{2\pi\alpha^2}(\log(r) + K_0(\alpha r))$$

In this case, the velocity expression contains a logarithmic singularity that can be regularized by replacing r with $R = \sqrt{r^2 + \delta^2}$ as in the approach of Section 2.1.

Acknowledgements

K. Leiderman was funded by the NSF Grant DMS-0540779; R. Cortez was partially funded by NSF Grant DMS-0612625, B. Cummins was partially supported by NSF CMMI Grant 0849433.

References

[1] J.T. Beale, A convergent boundary integral method for three-dimensional water waves, Math. Comp. 70 (2001) 977–1029.
[2] H.C. Brinkman, A calculation of the viscous force exerted by a flowing fluid on a dense swarm of particles, Appl. Sci. Res A1 (1947) 27–34.
[3] A.Y.L. Cheer, M.A.R. Koehl, Paddles and rakes: fluid flow through bristled appendages of small organisms, J. Theor. Biol. 129 (1987) 17–39.
[4] R. Cortez, The method of regularized stokeslets, SIAM J. Sci. Comput. 23 (4) (2001) 1204–1225.
[5] Q. Du, M. Gunzburger, L. Ju, Constrained centroidal voronoi tessellations for surfaces, SIAM J. Sci. Comput. 24 (2003) 1488–1506.
[6] L. Durlofsky, J.F. Brady, Analysis of the Brinkman equation as a model for flow in porous media, Phys. Fluids 30 (11) (1987) 3329–3341.
[7] J. Feng, P. Ganatos, S. Weinbaum, Motion of a sphere near planar confining boundaries in a Brinkman medium, J. Fluid Mech. 375 (1998) 265–296.
[8] R. Ganapathy, Creeping flow past a solid sphere in a porous medium, ZAMM 77 (11) (1997) 871–875.
[9] I.D. Howells, Drag on fixed beds of fibres in slow flow, J. Fluid Mech. 355 (1998) 163–192.
[10] Khodor Khadra, Philippe Angotb, Sacha Parneixc, Jean-Paul Caltagirone, Fictitious domain approach for numerical modelling of navier–stokes equations, Int. J. Numer. Meth. Fluids 34 (2000) 651–684.
[11] MAR Koehl, Hairy little legs: feeding, smelling, and swimming at low Reynolds numbers, Fluid Dynamics in Biology: Proceedings of an AMS-IMS-SIAM Joint Summer Research Conference held July 6–12, 1991 with Support from the National Science Foundation and NASA Headquarters, 141, Amer Mathematical Society, 1993, p. 33.
[12] M.A.R. Koehl, J.R. Strickler, Copepod feeding currents: food capture at low Reynolds number, Limnol. Oceanogr. 26 (6) (1981) 1062–1073.
[13] AM Leshansky, Enhanced low Reynolds number propulsion in heterogeneous viscous environment, 2009, Arxiv preprint arXiv:0910.3579.
[14] J.R. Looker, S.L. Carnie, The hydrodynamics of an oscillating porous sphere, Phys. Fluids 16 (1) (2004) 62–72.
[15] I. Pop, D.B. Ingham, Flow past a sphere embedded in a porous medium based on the brinkman model, Int. Comm. Heat Mass Transfer 23 (6) (1996) 865–874.
[16] H.J. Price, G.A. Paffenhofer, J.R. Strickler, Modes of cell capture in calanoid copepods, Limnol. Oceanogr. 28 (1) (1983) 116–123.
[17] R. Renka, Algorithm 772, stripack: Delaunay triangulation and voronoi diagrams on the surface of a sphere, ACM Trans. Math. Soft. 23 (1997) 416–434.
[18] T.W. Secomb, R. Hsu, A.R. Pries, A model for red blood cell motion in glycocalyx-lined capillaries, Amer. J. Physio. Heart Circ. Physiol. 274 (1998) 1016–1022.
[19] M. Shoji, H. Okamoto, T. Ooura, Particle trajectory around a running cylinder or a sphere, Fluid Dyn. Res. 42 (2009) 025506.

[20] Y.E. Solomentsev, J.L. Anderson, Rotation of a sphere in brinkman fluids, Phys. Fluids 8 (4) (1995) 1119–1121.
[21] M. Sugihara-Seki, Motion of a sphere in a cylindrical tube filled with a Brinkman medium, Fluid Dynam. Res. 34 (2004) 59–76, doi:10.1016/j.fluiddyn.2003.08.007.
[22] C.C. Tsai, Solutions of slow brinkman flows using the method of fundamental solutions, Int. J. Numer. Meth. Fluids 56 (2008) 927–940.
[23] M. Vanni, Creeping flow over spherical permeable aggregates, Chem. Eng. Sci. 55 (2000) 685–698.
[24] R. Čiegis, O. Iliev, Z. Lakdawala, On parallel numerical algorithms for simulating industrial filtration problems, Comput. Meth. Appl. Math. 7 (2) (2007) 118–134.